













Research Article

Studies on Synthesis and Characterization of $\text{Fe}_3\text{O}_4@\text{SiO}_2@\text{Ru}$ Hybrid Magnetic Composites for Reusable Photocatalytic Application

Avvaru Praveen Kumar ¹, Dinesh Bilehal ², Tegene Desalegn ¹, Shalendra Kumar ^{3,4},
Faheem Ahmed ³, H. C. Ananda Murthy ¹, Deepak Kumar ⁵, Gaurav Gupta ⁶,
Dinesh Kumar Chellappan ⁷, Sachin Kumar Singh ⁸, Kamal Dua ^{9,10}
and Yong-Ill Lee ¹¹

¹Department of Applied Chemistry, School of Applied Natural Science, Adama Science and Technology University, P.O. Box 1888, Adama, Ethiopia

²Department of Chemistry, Karnatak University, Dharwad, 560008 Karnataka, India

³Department of Physics, College of Science, King Faisal University, P.O. Box 400, Al-Ahsa 31982, Saudi Arabia

⁴Department of Physics, University of Petroleum and Energy Studies, Dehradun 248007, India

⁵Department of Pharmaceutical Chemistry, School of Pharmaceutical Sciences, Shoolini University, 173229, Solan, Himachal Pradesh, India

⁶Department of Pharmacology, School of Pharmacy, Suresh Gyan Vihar University, Mahal Road, Jagatpura, Jaipur, India

⁷Department of Life Sciences, School of Pharmacy, International Medical University, Bukit Jalil, Kuala Lumpur 57000, Malaysia

⁸School of Pharmaceutical Sciences, Lovely Professional University, Phagwara, 144411 Punjab, India

⁹Discipline of Pharmacy, Graduate School of Health, University of Technology Sydney, NSW 2007, Australia

¹⁰Faculty of Health, Australian Research Centre in Complementary and Integrative Medicine, University of Technology Sydney, Ultimo, Australia

¹¹Department of Chemistry, Changwon National University, Changwon 51140, Republic of Korea

Correspondence should be addressed to Avvaru Praveen Kumar; drkumar.kr@gmail.com

Received 24 September 2021; Revised 13 December 2021; Accepted 14 December 2021; Published 10 January 2022

Academic Editor: Silvano Mignardi

Copyright © 2022 Avvaru Praveen Kumar et al. This is an open access article distributed under the Creative Commons Attribution License, which permits unrestricted use, distribution, and reproduction in any medium, provided the original work is properly cited.

Degradation of dye pollutants by the photocatalytic process has been regarded as the most efficient green method for removal of organic dyes from contaminated water. The current research work describes the synthesis of $\text{Fe}_3\text{O}_4@\text{SiO}_2@\text{Ru}$ hybrid magnetic composites (HMCs) and their photocatalytic degradation of two azo dye pollutants, methyl orange (MO) and methyl red (MR), under irradiation of visible light. The synthesis of $\text{Fe}_3\text{O}_4@\text{SiO}_2@\text{Ru}$ HMCs involves three stages, including synthesis of Fe_3O_4 magnetic microspheres (MMSs), followed by silica (SiO_2) coating to get $\text{Fe}_3\text{O}_4@\text{SiO}_2$ MMSs, and then incorporation of presynthesized Ru nanoparticles (~3 nm) onto the surface of $\text{Fe}_3\text{O}_4@\text{SiO}_2$ HMCs. The synthesized HMCs were characterized by XRD, FTIR, TEM, EDS, XPS, BET analysis, UV-DRS, PL spectroscopy, and VSM to study the physical and chemical properties. Furthermore, the narrow band gap energy of the HMC photocatalyst is a significant parameter that provides high photocatalytic properties due to the high light adsorption. The photocatalytic activity of synthesized $\text{Fe}_3\text{O}_4@\text{SiO}_2@\text{Ru}$ HMCs was assessed by researching their ability to degrade the aqueous solution of MO and MR dyes under visible radiation, and the influence of various functional parameters on photocatalytic degradation has also been studied. The results indicate that the photocatalytic degradation of MO and MR dyes is more than 90%, and acid media favors better degradation. The probable mechanism of photodegradation of azo dyes by $\text{Fe}_3\text{O}_4@\text{SiO}_2@\text{Ru}$ HMC catalysts has been proposed. Furthermore, due to the strong ferromagnetic Fe_3O_4 core, HMCs were easily separated from the solution after the photocatalytic degradation process for reuse. Also, the photocatalytic activity after six cycles of use is greater than 90%, suggesting the stability of the synthesized $\text{Fe}_3\text{O}_4@\text{SiO}_2@\text{Ru}$ HMCs.

1. Introduction

The increased toxicity and carcinogenicity of toxic contaminants released from industrial effluents have created significant environmental problems. Organic dyes have been used to color fabrics since ancient times and are manufactured in large quantities (nearly 10,000 different styles with over 700,000 metric tons in industrial production) [1]. Approximately 10%–15% of dyes are wasted during production processes, and clothes can only absorb 25% dye on their surface [2]. In general, fibers (54 percent) are the largest emitters of dye effluents, led by dyeing (21 percent), paper (10 percent), and paint (8 percent) industries [3]. Wastewater containing synthetic dyes, even in trace amounts, has been identified as the primary cause of aquatic life destruction. The majority of synthetic dyes are hazardous to health (a handful are carcinogenic) and impossible to degrade [4, 5]. Methyl orange (MO) dye is one of the most widely used azo dyes in the clothing, dairy, leather, and pharmaceutical industries. Additionally, MO is used as a coloring agent. The most detrimental effects of MO use are toxicity, mutagenicity, and carcinogenicity [6]. Methyl Red is a well-known dye that has been widely used in garment dyeing and paper printing [7]. If inhaled/swallowed, it induces irritation of the skin and eyes, as well as discomfort of the respiratory and digestive tracts. It has been suspected as a possible carcinogen and mutagen.

To eliminate the harmful effects of dyes and similar substances, effluents released from different industries should be handled with effective (low-cost and/or easy-to-handle) nanomaterial-based technologies. Additionally, removing dyes from the atmosphere is critical for making water supply accessible to living organisms. Adsorption, filtration, coagulation, and biodegradation are all traditional processes used in the water treatment industry [8, 9]. These approaches have limitations in terms of cost, feasibility, time required, and environmental impacts. Despite the fact that adsorption is a common process for removing toxic textile dyes, it could be incapable of degrading or mineralizing organic contaminants from the environment.

Among the different methods, photodegradation using semiconductor metal oxides is a potential green environmental protection technique because it can directly break down dye molecules in the effluent to harmless ones such as CO_2 and H_2O [10, 11]. Due to its low cost, it has been extensively employed to remove organic dye molecules from water [12–15]. To remove organic pollutants from wastewater, a number of semiconductor photocatalytic materials such as ZnO , TiO_2 , and Fe_2O_3 have been utilized [16, 17]. Additionally, semiconductor photocatalysts can exhibit considerable efficiency and high catalytic activity when combined with a variety of other materials [18]. Through integrating nanoparticles (NPs) of diverse components into a single object, the individual capabilities obtained from each component's particular electrical, mechanical, optical, and catalytic properties may be merged [19, 20]. As a result, these multicomponent NPs have found broad usage in a wide number of sectors [21, 22]. For example, magnetic materials are often mixed with noble metal NPs, allowing the noble metal NPs to be easily separated from the mixtures using merely an external mag-

netic field, giving reusable photocatalysts [23, 24]. Nevertheless, these hybrid NPs agglomerate quickly, significantly decreasing their initial action [25]. In addition, bare iron oxide NPs demonstrate a high degree of chemical activity and are quickly oxidized in the air (particularly magnetite), resulting in the loss of magnetism and disparity [26]. As a result, it is important to optimize the stability of composite nanomaterials. Thus, it is important to improve the stability and compatibility of nanomaterials. Fortunately, surface coating is an excellent alternative technology. Carbon, polymers, and silica are the most frequently used coating materials in the literature [27, 28].

Transition metal/oxide nanomaterials and also their composites exhibit excellent catalytic and photocatalytic activities [29–32]. The transition-based nanomaterials show desirable characteristics like large surface area to volume ratio compared to the bulk, well-controlled structures, and as semiconductors with wide band gaps, nontoxicity, and high stability in aqueous solution which make them useful not only in catalytic applications but also in a wide range of applications such as chemical sensing [33], electrochemical energy conversion and storage [34], solar cells [35], discrimination of racemic drugs [36], sustainable environmental remediation and pollutant sensing [37], and biological applications [38]. Photodegradation of dyes is a standard process for determining the catalytic action of different types of photocatalysts. In the literature, many research works have been published on ruthenium NPs in either dispersed or immobilized state for catalytic applications. However, some methods were reported on magnetic $\text{Ru}/\text{Fe}_3\text{O}_4/\text{SiO}_2$ nanospheres to prepare cispinane [25], Ru NPs decorated with $\text{Fe}_3\text{O}_4/\text{SiO}_2\text{-NH}_2$ core-shell microspheres for hydrogen production [39], $\text{Fe}_3\text{O}_4/\text{SiO}_2/\text{APTS}/\text{Ru}$ magnetic nanocomposite catalyst for hydrogenation reactions [40], and $\text{Fe}_3\text{O}_4/\text{C}/\text{Ru}$ hybrid composites for photocatalytic degradation of methylene blue under visible light [41]. The current study describes the synthesis and fabrication of silica-coated magnetic iron oxide core-shell microspheres with ruthenium (Ru) nanoparticles to obtain $\text{Fe}_3\text{O}_4/\text{SiO}_2/\text{Ru}$ hybrid magnetic composites (HMCs). The incorporated Ru NPs onto the magnetic silica are expected to reduce the band gap, which could promote enhancing photocatalytic property. To the best of our knowledge, the use of $\text{Fe}_3\text{O}_4/\text{SiO}_2/\text{Ru}$ HMCs as photocatalysts has not been reported. The morphological, optical, and magnetic properties of $\text{Fe}_3\text{O}_4/\text{SiO}_2/\text{Ru}$ HMCs were investigated by different characterization methods. In this work, two azo organic pollutants, methyl orange and methyl red, were selected for their degradation in an aqueous medium under visible light radiation to evaluate the photocatalytic performance of the prepared HMCs.

2. Experimental

2.1. Materials. $\text{FeCl}_3 \cdot 6\text{H}_2\text{O}$, sodium acetate, sodium acrylate, and ammonium hydroxide (NH_4OH) were received from Sigma. The azo dyes, methyl orange (MO) and methyl red (MR), ruthenium(III) acetylacetonate, ethylene glycol, poly(vinylpyrrolidone), 1,4-butanediol, and tetraethyl orthosilicate (TEOS) were supplied by Sigma-Aldrich. Ethanol (EtOH) of HPLC grade was obtained from J. T. Baker. Other chemicals

of the analytical reagent grade were employed, which had a purity of more than 99% and were used without additional purification.

2.2. Synthesis of Fe_3O_4 Magnetic Microspheres. The Fe_3O_4 magnetic microsphere (MMS) synthesis was carried out by solvothermal process as per previous report [42]. Briefly, in 100 mL ethylene glycol, 2 g of $FeCl_3 \cdot 6H_2O$, 5.5 g of sodium acetate, and 5.5 g of sodium acrylate were dissolved with magnetic stirring at room temperature for 90 min. The resultant solution obtained was then transferred into a Teflon-lined stainless steel autoclave (200 mL in capacity) for heating at 200°C for 10 h. After the reaction time, the autoclave was cooled to room temperature, and the obtained black product of Fe_3O_4 magnetic microspheres was thoroughly washed with deionized H_2O and EtOH for several times and finally vacuum dried at room temperature.

2.3. Synthesis of $Fe_3O_4@SiO_2$ Core-Shell MMSs. At room temperature, the Fe_3O_4 MMSs (50 mg) were dispersed in a solution comprising 50 mL of EtOH, 20 mL of H_2O , and 2.0 mL of NH_3 solution, and the solution was homogenized by ultrasonication. Then, TEOS was added through injection, and the resultant dispersion solution was mechanically stirred for 2 h at room temperature. The product obtained as $Fe_3O_4@SiO_2$ MMSs was collected by applying an external magnetic field (using a magnet) and washed several times with deionized water and EtOH.

2.4. Synthesis of $Fe_3O_4@SiO_2@Ru$ HMCs. To synthesize $Fe_3O_4@SiO_2@Ru$ HMCs, first, Ru NPs of 3 nm size were synthesized by the reported procedure [43]. To immobilize the synthesized Ru NPs onto the $Fe_3O_4@SiO_2$ core-shell MMSs, the following procedure was employed. Initially, 0.5 mL of acetic acid solution was added to an ethanolic solution of 50 mg mL⁻¹ of $Fe_3O_4@SiO_2$ magnetic sample at room temperature, followed by sonication for 30 min. This procedure was implemented to activate the surface of $Fe_3O_4@SiO_2$ core-shell MMSs. Then, a solution of already synthesized Ru NPs (dispersed in EtOH) was added to the $Fe_3O_4@SiO_2$ core-shell MMSs (5 mL), and the solution was ultrasonicated at room temperature for 60 min. During this process, the Ru NPs were immobilized on the surface of the $Fe_3O_4@SiO_2$ MMSs to obtain $Fe_3O_4@SiO_2@Ru$ HMCs. This final product of Ru magnetic composite was isolated from the solution by a magnet, then rinsed several times with H_2O and EtOH, and then dispersed in H_2O for characterization and photocatalytic degradation of azo dyes.

2.5. Characterization of the Samples. The XRD (X-ray diffraction) pattern of all the samples was carried out by Philips X'pert MPD 3040 with Cu K α radiation over a 2 θ range from 20° to 80° at 2.5° per minute. Fourier transform infrared (FTIR) spectra were obtained using a Nicolet FT-IR 400 spectrophotometer (Nicolet iS10, SCINCO, USA) using the KBr pellet method. The morphology and size of all magnetic microspheres and composites were recorded by a transmission electron microscope (TEM) (JEM-2100F, JEOL, Japan). TEM-EDX (energy-dispersive X-ray) analysis was used to determine the elemental analysis of $Fe_3O_4@SiO_2@Ru$ mag-

netic composite sample. The XPS (X-ray photoelectron spectroscopy) was recorded by a MultiLab2000 (Thermo VG Scientific, USA). The pore size distributions, pore volume, and surface area were determined by N_2 adsorption-desorption isotherms using Autosorb-1 equipment (Quantachrome, USA). The pore size distribution and surface area were measured by the Brunauer–Emmett–Teller (BET) method. A vibrating sample magnetometer (VSM, Lakeshore 7304) was employed to determine the magnetic properties of the Fe_3O_4 , $Fe_3O_4@SiO_2$, and $Fe_3O_4@SiO_2@Ru$ magnetic microsphere samples at room temperature. The UV-Vis spectra were acquired by a Lambda 950 spectrometer (PerkinElmer). A Shimadzu UV-2600 spectrophotometer was used for UV-Vis DRS analyses. The fluorescence spectra of the magnetic samples were recorded using a Shimadzu, RF-5301PC spectrofluorophotometer.

2.6. Photocatalytic Degradation. The photocatalytic activity performances of synthesized $Fe_3O_4@SiO_2@Ru$ HMCs were examined for their ability to remove two azo dyes, MO and MR, in an aqueous solution under visible light. In a typical photocatalytic degradation process, a magnetic composite photocatalyst of 10 mg was added to a 50 mL of MO/MR dye aqueous solution (30 mg/L). Afterwards, the reaction solution was stirred in the dark for 60 min to attain the adsorption–desorption equilibrium of the MO/MR dye on the composite photocatalyst surface prior to visible-light irradiation. The same experimental procedure was used for control experiments. A homemade setup was used to conduct the photocatalytic experiments. A tungsten halogen lamp (300 W, 8500 lumen) was employed to generate visible light radiation. The photocatalytic degradation reaction was tracked at various time intervals by recording the absorbance at λ_{max} of the MO/MR dye at particular wavelengths using UV-Vis spectrophotometry. The photocatalytic degradation rate can be calculated as follows:

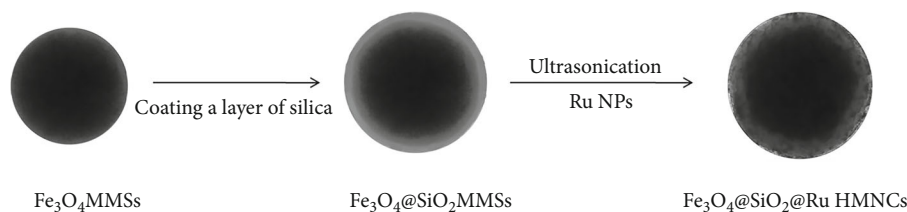
$$\text{Degradation rate (\%)} = \left[\frac{A_0 - A}{A_0} \right] \times 100, \quad (1)$$

$$\text{Degradation rate (\%)} = \left[\frac{C_0 - C}{C_0} \right] \times 100,$$

where A_0 indicates the initial absorbance of the MO/MR solution, A shows the absorbance of the MO/MR solution after visible-light irradiation at time t , C_0 is the initial concentration of the MO/MR solution, and C is the concentration of the dye solution after visible irradiation at time t .

3. Results and Discussion

3.1. Synthesis and Characterization. The $Fe_3O_4@SiO_2@Ru$ core-shell HMCs were synthesized in three steps. A scheme for the synthesis of $Fe_3O_4@SiO_2@Ru$ core-shell HMCs is shown in Scheme 1. In the first step, the Fe_3O_4 MMSs were prepared by the solvothermal method using Fe(III) salt as the sole iron seed for magnetic property, sodium acrylate as the reducing agent, NaAc as the precipitating agent, and ethylene glycol as the solvent. In the second step, silica-



SCHEME 1: Synthesis of Ru NP-decorated silica-coated iron oxide magnetic hybrid magnetic nanocomposites ($\text{Fe}_3\text{O}_4@\text{SiO}_2@\text{Ru}$ HMNCs).

coated magnetite ($\text{Fe}_3\text{O}_4@\text{SiO}_2$) MMSs were prepared by coating a layer of silica on the surface of Fe_3O_4 MMSs by hydrolysis and condensation of tetraethyl orthosilicate (TEOS) in a mixture of EtOH, ammonia, and water. The silica layer was coated on magnetic Fe_3O_4 MMSs to protect against photocorrosion and leaching of Fe ions. Moreover, this SiO_2 layer has a negative effect on the photocatalytic activity because it inhibits charge transfer between the Fe_3O_4 and the catalyst [44]. In the final third step, $\text{Fe}_3\text{O}_4@\text{SiO}_2@\text{Ru}$ core-shell HMCs were obtained by stabilization of presynthesized Ru NPs on to the surface of $\text{Fe}_3\text{O}_4@\text{SiO}_2$ MMSs. The obtained HMCs were characterized by different instrumental methods.

3.2. XRD Studies. XRD studies were conducted to examine the purity and crystallinity of the synthesized Fe_3O_4 MMSs, $\text{Fe}_3\text{O}_4@\text{SiO}_2$ MMSs, and $\text{Fe}_3\text{O}_4@\text{SiO}_2@\text{Ru}$ HMCs. The diffraction peaks of the Fe_3O_4 MMSs are clearly visible from Figure 1(a), detected at 2θ values, 30.1, 35.5, 43.2, 53.6, 57.3, 62.7, and 74.4, which can be assigned to (220), (311), (400), (422), (511), (440), and (533) planes, respectively, which are well matched with the face center-cubic phase of Fe_3O_4 (JCPDS card, File No. 19-0629). Furthermore, no peaks have been found specifically for impurities, indicating that the Fe_3O_4 MMSs synthesized by the solvothermal method are very pure. The XRD pattern of $\text{Fe}_3\text{O}_4@\text{SiO}_2$ MMSs and $\text{Fe}_3\text{O}_4@\text{SiO}_2@\text{Ru}$ HMCs exhibits reflection peaks similar to Fe_3O_4 MMSs. This suggests that the Fe_3O_4 magnetite phase is observed in all X-ray diffraction patterns, pointing that the crystal structure of Fe_3O_4 has not changed after coating the SiO_2 layer on the Fe_3O_4 and also even after incorporating Ru NPs on the SiO_2 layer. This is because of the fact that the SiO_2 layer on the magnetic Fe_3O_4 core is amorphous, and therefore, no characteristic peaks of SiO_2 are noticed in the XRD pattern. Nevertheless, the characteristic diffraction peaks of Fe_3O_4 are weakened due to the amorphous SiO_2 -coated layer on the surface of the magnetic Fe_3O_4 core. Moreover, the characteristic diffraction peaks of the metallic Ru are not observed in $\text{Fe}_3\text{O}_4@\text{SiO}_2@\text{Ru}$ HMCs, indicating that Ru NPs are in a uniformly distributed state with a size of ~ 3 nm, which is not within the XRD detection limit [45]. The XRD patterns of $\text{Fe}_3\text{O}_4@\text{SiO}_2$ MMSs and $\text{Fe}_3\text{O}_4@\text{SiO}_2@\text{Ru}$ HMCs also revealed that there were no other contaminants in those materials. XRD studies have shown the formation of highly pure Fe_3O_4 MMSs and also the purity of the $\text{Fe}_3\text{O}_4@\text{SiO}_2@\text{Ru}$ HMCs.

3.3. FT-IR Studies. The synthesized Fe_3O_4 , $\text{Fe}_3\text{O}_4@\text{SiO}_2$, and $\text{Fe}_3\text{O}_4@\text{SiO}_2@\text{Ru}$ composite samples were characterized by

FT-IR spectroscopy at room temperature to confirm their chemical composition. As shown in Figure 1(b), bare Fe_3O_4 MMSs show a characteristic absorption band at 591 cm^{-1} for stretching vibration of the Fe–O bond. The broad absorption band observed at approximately 3430 cm^{-1} is related to O–H stretching vibrations of the surface Fe–OH groups. The FT-IR spectrum of $\text{Fe}_3\text{O}_4@\text{SiO}_2$ MMSs displays characteristic asymmetric and symmetric linear stretching vibrations of the Si–O–Si bond, and those absorptions were appeared at 1082 and 798 cm^{-1} , respectively [46]. The absorption peaks for bending vibrations of Si–OH and Si–O–Si were observed at 948 and 461 cm^{-1} , respectively [47]. Apparently, these stretching and bending vibrations represent the SiO_2 (silica) layer successfully formed on the surface of superparamagnetic Fe_3O_4 MMSs.

3.4. TEM Studies. Figure 2 displays TEM images of superparamagnetic Fe_3O_4 and core-shell $\text{Fe}_3\text{O}_4@\text{SiO}_2$ MMSs. As shown in the TEM images, all the four images (a–d) appear to have a narrow size distribution and better monodispersity. It can be easily seen in Figures 2(a) and 2(b) that the Fe_3O_4 MMSs are almost spherical in shape and have an average diameter of *ca* 180 nm. From Figures 2(c) and 2(d), the core-shell structure of $\text{Fe}_3\text{O}_4@\text{SiO}_2$ is clearly visible, consisting of a dark black magnetic Fe_3O_4 core and its surface uniformly coated with a silica shell (grey colored) of thickness *ca* 40 nm. Using the sol-gel approach, it is possible to tune the thickness of the silica layer from tens to hundreds of nanometers [48]. The Ru NPs prepared by colloidal synthesis are ~ 3 nm in size and are well dispersed as seen in Figure 3(a). TEM images of the obtained $\text{Fe}_3\text{O}_4@\text{SiO}_2@\text{Ru}$ HMCs (Figures 3(b)–3(d)) indicate that the magnetic $\text{Fe}_3\text{O}_4@\text{SiO}_2@\text{Ru}$ composite microspheres are well dispersed and have an average diameter of 280 nm. As shown in Figures 3(b)–3(d), many monodispersed Ru NPs (~ 3 nm) are uniformly decorated, indicating that the synthesized Ru NPs are stabilized onto the surface of $\text{Fe}_3\text{O}_4@\text{SiO}_2$ MMSs to form $\text{Fe}_3\text{O}_4@\text{SiO}_2@\text{Ru}$ HMCs. Furthermore, these $\text{Fe}_3\text{O}_4@\text{SiO}_2@\text{Ru}$ HMCs were stable and did not decompose even after 150 minutes of sonication. This ensures that deposited Ru NPs are not easily lost when reused in liquid-phase catalytic reactions [49].

Additional TEM studies were performed in conjunction with EDX spectrum analysis for positive identification of synthesized $\text{Fe}_3\text{O}_4@\text{SiO}_2@\text{Ru}$ HMCs. From the TEM–EDX spectrum shown in Figure 4, a good correspondence of the elemental distribution of Fe, O, and Si can be clearly seen and confirmed the presence of metallic Ru content in the $\text{Fe}_3\text{O}_4@\text{SiO}_2@\text{Ru}$ magnetic composite sample.

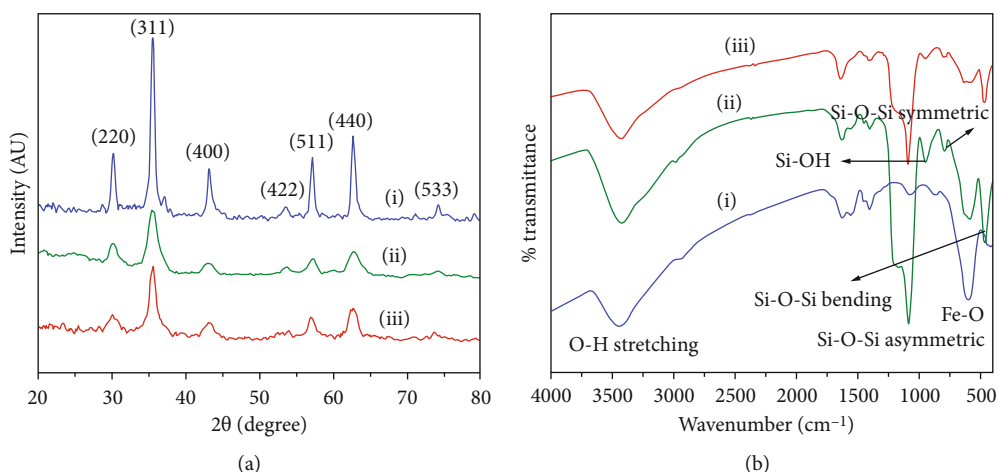


FIGURE 1: (a) XRD patterns and (b) FT-IR spectra of (i) Fe_3O_4 MMSs, (ii) $\text{Fe}_3\text{O}_4@SiO_2$ MMSs, and (iii) $\text{Fe}_3\text{O}_4@SiO_2@Ru$ HMCs.

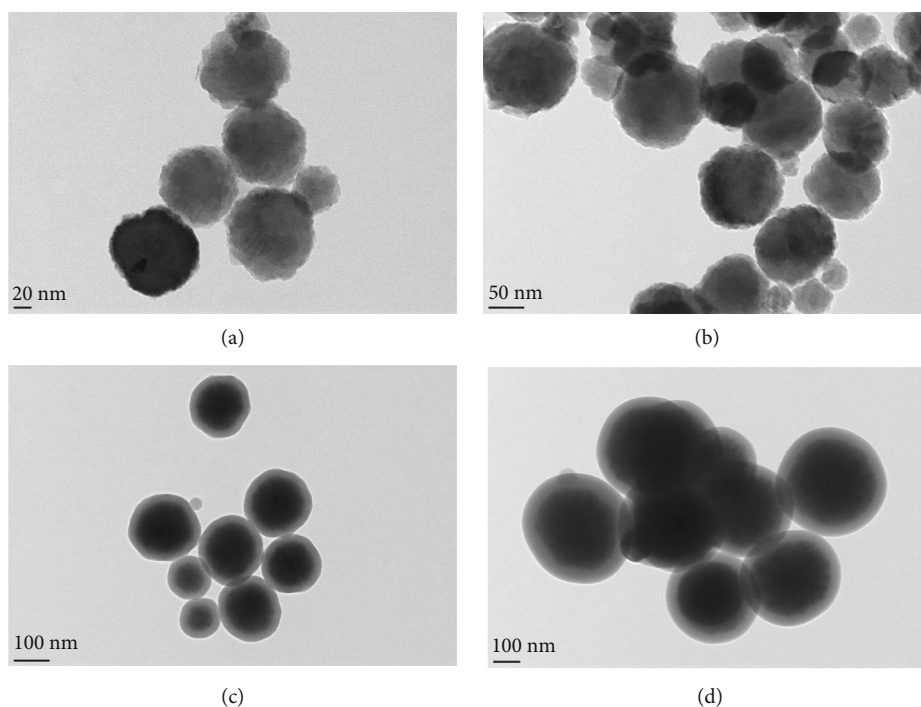


FIGURE 2: TEM images of (a, b) Fe_3O_4 MMSs and (c, d) $\text{Fe}_3\text{O}_4@SiO_2$ MMSs.

3.5. XPS Studies. The $\text{Fe}_3\text{O}_4@SiO_2@Ru$ composite was also characterized by XPS in order to ensure the existence of decorated ruthenium content and its oxidation state. The HR-XPS results of the $\text{Fe}_3\text{O}_4@SiO_2@Ru$ HMC are presented in Figure 5. The HR-XPS spectrum of Fe (Figure 5(a)) exhibits peaks at the binding energies of 711.3 and 725.1 eV belonging to $\text{Fe}_{3/2}$ and $\text{Fe}_{1/2}$, respectively, in the 2p region [50, 51]. As shown Figure 5(b), the binding energy at 531 eV was assigned to O 1s. The HR-XPS spectrum of Figure 5(c) represents Ru in the 3p region and exhibits two peaks at binding energies of 461.4 and 483.2 eV, which are characteristic of $\text{Ru}_{3/2}$ and $\text{Ru}_{1/2}$, respectively. Doublet at binding energies, 284.0 and 297.2 eV (Figure 6(d)) were ascribed to $\text{Ru}(0)$ $3d_{3/2}$ and

$3d_{5/2}$, respectively. These HR-XPS results confirm the presence of ruthenium in its metallic state on the surface of $\text{Fe}_3\text{O}_4@SiO_2$ MMSs [52, 53].

3.6. BET Analysis. The specific surface area and pore size distribution of as-synthesized $\text{Fe}_3\text{O}_4@SiO_2@Ru$ HMCs were determined by N_2 adsorption–desorption analysis. Figure 6 provides the N_2 adsorption–desorption isotherms and the corresponding pore-size distribution curve, suggesting that the $\text{Fe}_3\text{O}_4@SiO_2@Ru$ composite exhibits a typical IV isotherm with a H3-type hysteresis loop (P/P_0 of 0.38) (Figure 6(a)), and this supports the presence of well-defined mesopores [54]. The BET specific surface area and

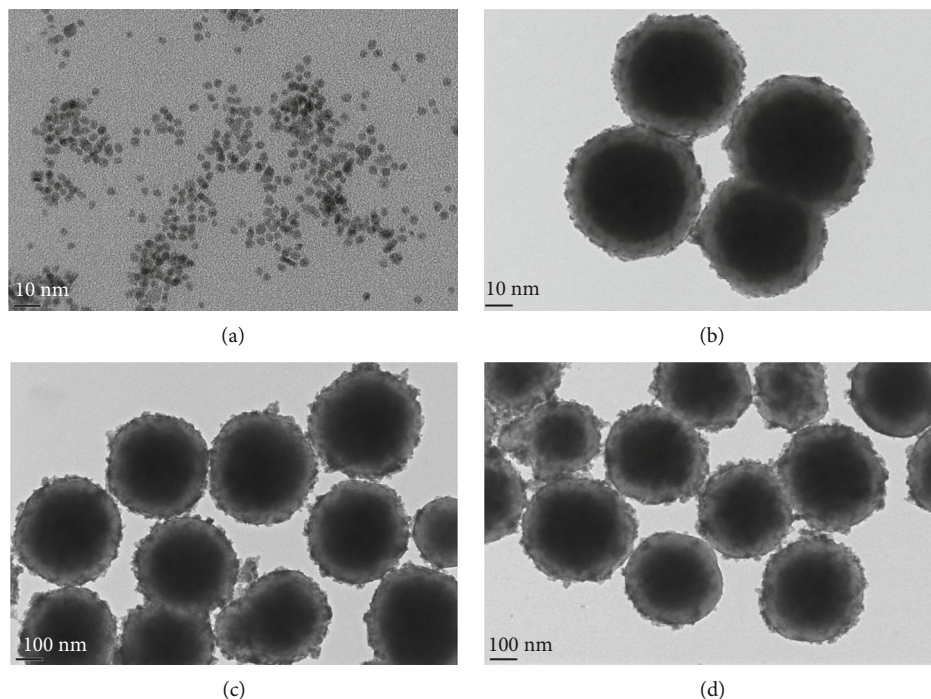


FIGURE 3: TEM images of (a) Ru NPs and (b–d) $\text{Fe}_3\text{O}_4@\text{SiO}_2@\text{Ru}$ HMCs.

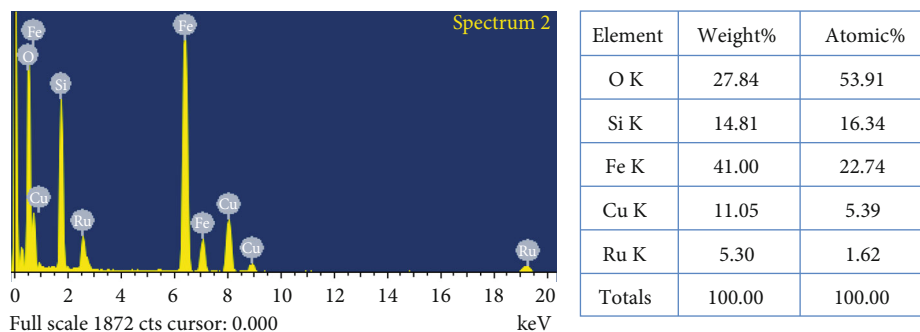


FIGURE 4: TEM-EDX spectrum of $\text{Fe}_3\text{O}_4@\text{SiO}_2@\text{Ru}$ HMCs.

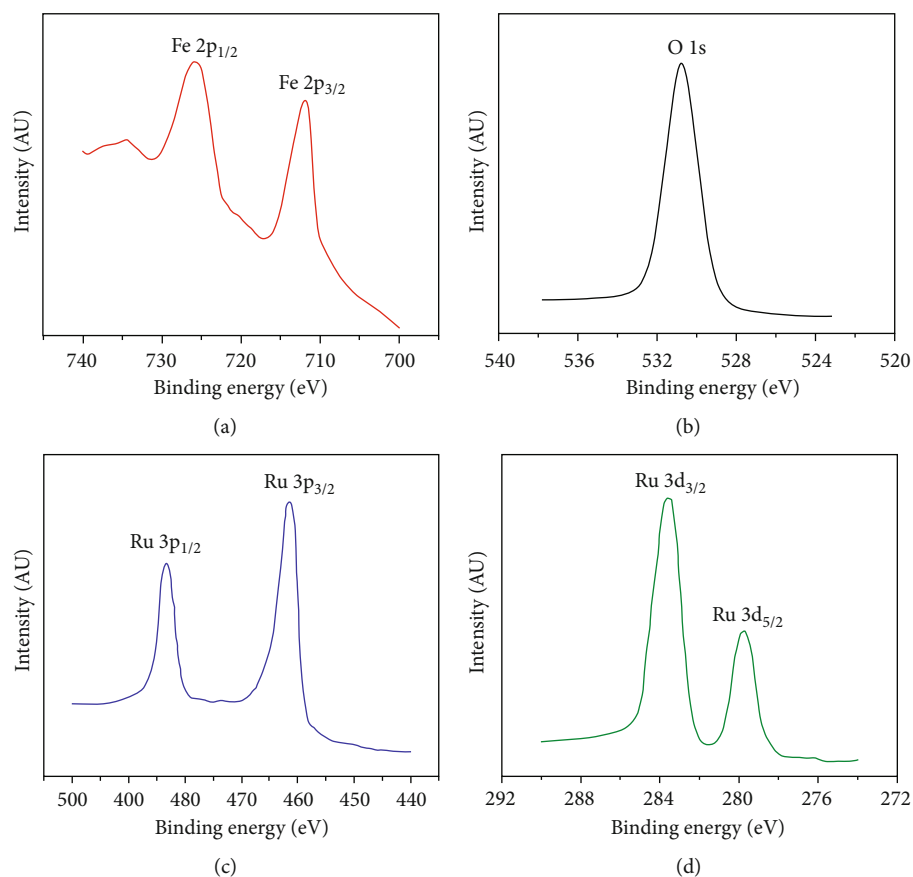
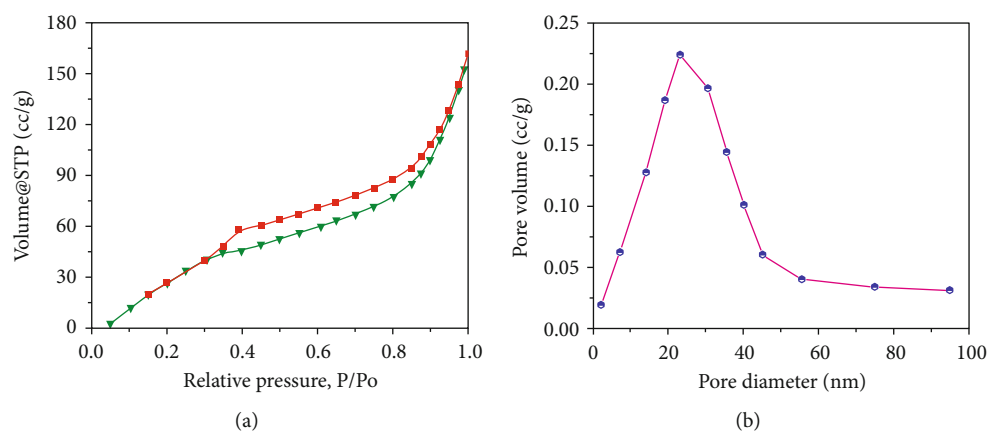
pore volume were measured as $93.24 \text{ m}^2/\text{g}$ and $0.18 \text{ cm}^3/\text{g}$, respectively. Figure 6(b) displays the pore size distribution plot, which refers to well-developed mesopores with a diameter of 22.98 nm according to the BJH model, which support the porous nature of the deposited Ru NPs. This is important not only for the exposure of active adsorption sites and provides more efficient transport pathways but also to facilitate increasing photocatalytic performance.

3.7. UV-Vis (DRS) Analysis. UV-Vis DRS was performed to study the optical absorption behavior of the synthesized Fe_3O_4 MMS, $\text{Fe}_3\text{O}_4@\text{SiO}_2$ MMS, and $\text{Fe}_3\text{O}_4@\text{SiO}_2@\text{Ru}$ composite samples. As shown in Figure 7(a), all magnetic samples show wide absorption and a strong absorptive peak at a wavelength of 410 nm . Moreover, the $\text{Fe}_3\text{O}_4@\text{SiO}_2@\text{Ru}$ HMC showed a wider absorption peak and a higher intensity of the absorption maxima with red-shift as compared to bare Fe_3O_4 MNSs and $\text{Fe}_3\text{O}_4@\text{SiO}_2$ MNSs. This demonstrates that the incorporated Ru NPs on the surface of $\text{Fe}_3\text{O}_4@\text{SiO}_2$

could significantly absorb visible light, which promotes more electron-hole pairs for greater photocatalytic activity. The band gap energy of $\text{Fe}_3\text{O}_4@\text{SiO}_2@\text{Ru}$ HMC was calculated by Tauc and Davis-Mott relation [55] as given below.

$$(\alpha h\nu)^n = K(h\nu - E_g), \quad (2)$$

where α is the absorption coefficient, $h\nu$ is the incident photon energy, K is the energy independent constant, E_g is the band gap energy, and $n = 1/2$ corresponding to the allowed direct transitions. The E_g is calculated from the plotting $(\alpha h\nu)^{1/2}$ against ν , by extrapolating the straight line portion of the curve to zero coefficient value. The Tauc plot (Figure 7(b)) showed that the band gap energies for Fe_3O_4 , $\text{Fe}_3\text{O}_4@\text{SiO}_2$, and $\text{Fe}_3\text{O}_4@\text{SiO}_2@\text{Ru}$ HMCs were 2.45 , 2.18 , and 2.03 eV , respectively. This clearly confirmed the band's red-shifts during the incorporation of Fe_3O_4 and also indicated that the visible light harvesting efficiency of Ru

FIGURE 5: HR-XPS spectra of Fe₃O₄@SiO₂@Ru HMCs.FIGURE 6: (a) N₂ adsorption-desorption isotherms and (b) pore size distribution of Fe₃O₄@SiO₂@Ru HMCs.

NP-decorated Fe₃O₄@SiO₂ HMCs for photocatalytic applications could be improved.(a)(b)

3.8. Photoluminescence (PL) Spectral Analysis. PL spectral analysis provides important and selective information about the efficiency of charge carrier trapping, migration, transfer, separation, and recombination processes of the photoinduced electron-hole pairs in the nanocatalysts [56, 57]. PL emission takes place as the electron comes from the excited state to the ground state. So, the PL intensity is directly pro-

portional to the separation of photoinduced charge carriers; therefore, the lower PL intensity reflects a decrease in the recombination probability [58]. The PL spectra of Fe₃O₄ MNSs, core-shell Fe₃O₄@SiO₂ MNSs and Fe₃O₄@SiO₂@Ru composite were carried out with an excitation of 300 nm at room temperature. As seen in Figure 8, all the samples of MMSs were exhibited similar spectral pattern in their emission. A major emission peak was observed at 465 nm of highest peak intensity and variations of PL intensity associated with the recombination rate of excited electron-hole

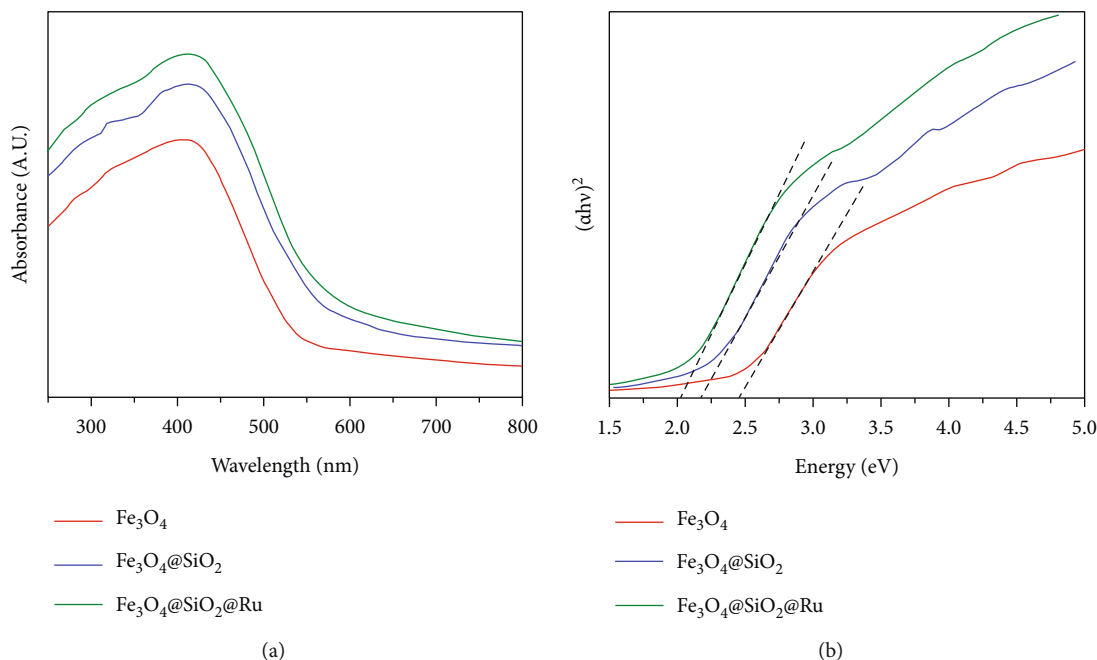


FIGURE 7: (a) UV-Vis DRS and (b) Tauc plots of Fe₃O₄ MMSs, Fe₃O₄@SiO₂ MMSs, and Fe₃O₄@SiO₂@Ru HMCs.

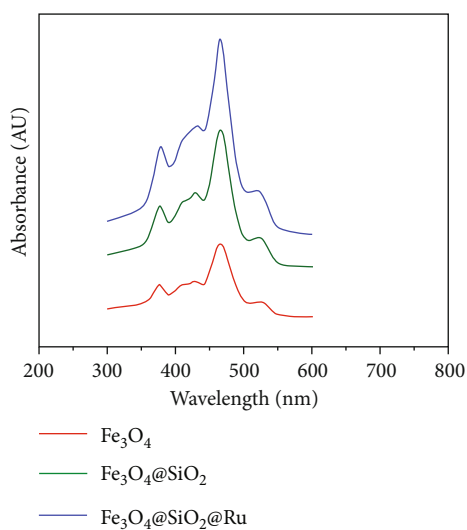


FIGURE 8: PL spectra of Fe₃O₄ MMSs, Fe₃O₄@SiO₂ MMSs, and Fe₃O₄@SiO₂@Ru HMCs.

pairs. The PL intensity decreased remarkably from Fe₃O₄ MMSs, Fe₃O₄@SiO₂ MMSs and Fe₃O₄@SiO₂@Ru composite, and Fe₃O₄@SiO₂@Ru composite notices lower emission intensity than pure magnetic Fe₃O₄ and core-shell Fe₃O₄@SiO₂ MMSs. This indicates that decorated Ru NPs further decreased the PL intensity which lowers the recombination rate and high separation efficiency of the photoinduced electron-hole pairs. Because the ability to separate (separation efficiency) photoinduced electron-hole pairs is one of the most significant parameters for photocatalytic activity, a low recombination rate is expected for high photocatalytic degradation potential. Therefore, it could be concluded that the Ru-decorated Fe₃O₄@SiO₂ composite contributes a large

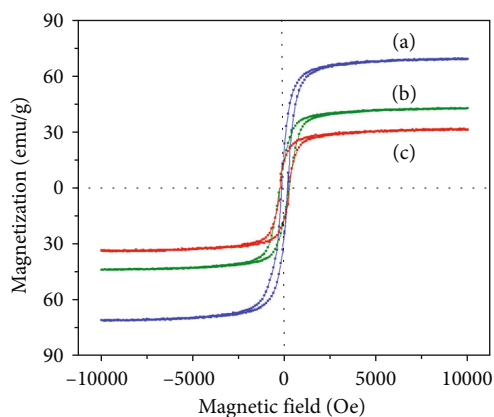
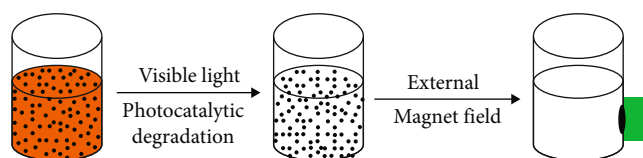


FIGURE 9: Magnetization curves of (a) Fe₃O₄ MMSs, (b) Fe₃O₄@SiO₂ MMSs, and (c) Fe₃O₄@SiO₂@Ru HMCs.

number of photoinduced electrons and holes which promote the photochemical transformation for the enhancement in the photocatalytic activity.

3.9. Magnetic Properties. To study the magnetic behavior, the magnetic properties of the prepared Fe₃O₄, core-shell Fe₃O₄@SiO₂, and Fe₃O₄@SiO₂@Ru HMCs were determined at room temperature using VSM. The curves of magnetization versus magnetic field (M-H loop) are displayed in Figure 9. All magnetic samples exhibit negligible hysteresis at the room-temperature magnetization, which reveals their super-paramagnetic behavior. The magnetic saturation values of bare Fe₃O₄ MMSs, core-shell Fe₃O₄@SiO₂ MMSs, and Fe₃O₄@SiO₂@Ru HMCs were measured as 68.78, 42.36, and 31.82 emu g⁻¹, respectively, which indicate a decrease in the magnetization after surface coating by the silica layer and the decorated Ru NPs. This decrease of magnetic



SCHEME 2: Decolorization of azo dyes by $\text{Fe}_3\text{O}_4@\text{SiO}_2@\text{Ru}$ photocatalysts.

saturation can be explained by considering the diamagnetic contribution of the silica shell and Ru NPs surrounding Fe_3O_4 [59]. The super-paramagnetic property of the $\text{Fe}_3\text{O}_4@\text{SiO}_2@\text{Ru}$ HMCs allows an easy and effective way to separate and recycle from catalytic reaction systems.

3.10. Photocatalytic Degradation of MO and MR Dyes. The organic dyes are the most common organic pollutants from dye industries to pollute water, so these dyes are one of the most marked analytes in water analysis. Photodegradation of dyes is a standard process for determining the catalytic action of different types of photocatalysts. In this work, fabricated $\text{Fe}_3\text{O}_4@\text{SiO}_2@\text{Ru}$ HMCs were applied as photocatalysts for the degradation of two azo dyes (MO and MR dyes) under visible light. Scheme 2 displays the decolorization of the MO azo dye solution using synthesized $\text{Fe}_3\text{O}_4@\text{SiO}_2@\text{Ru}$ HMCs.

Figure 9 illustrates the photocatalytic activity of $\text{Fe}_3\text{O}_4@\text{SiO}_2@\text{Ru}$ HMCs for the degradation of MO (Figure 9(a)) and MR (Figure 9(b)) dyes when exposed to visible light at different irradiation times at room temperature. Photodegradation of the azo dyes showed similar trend, where catalytic degradation rates increase over time and both azo dyes degrade by more than 90% (MO: 95% and MR 91%) within 150 min irradiation time. These findings indicate that $\text{Fe}_3\text{O}_4@\text{SiO}_2@\text{Ru}$ HMCs exhibit a higher photocatalytic performance when exposed to visible light. Control experiments on azo dyes were performed in the absence of $\text{Fe}_3\text{O}_4@\text{SiO}_2@\text{Ru}$ photocatalysts and in the presence of $\text{Fe}_3\text{O}_4@\text{SiO}_2$ MMSs to assess the photodegradation active component of the catalyst. As shown in Figure 10, almost no dye degradation was observed in the absence of $\text{Fe}_3\text{O}_4@\text{SiO}_2@\text{Ru}$ photocatalysts, and 7-8% degradation was detected using $\text{Fe}_3\text{O}_4@\text{SiO}_2$ MMSs. This suggests that very poor photocatalytic degradations occur except using $\text{Fe}_3\text{O}_4@\text{SiO}_2@\text{Ru}$ HMCs. Apart from this, an experiment was conducted using $\text{Fe}_3\text{O}_4@\text{SiO}_2@\text{Ru}$ HMCs in dark conditions to confirm that there is no photocatalytic degradation of azo dyes. The results found that the azo dye degradation was very poor, so it is negligible. These experimental results explore that the photocatalytic reaction is triggered and facilitated by the $\text{Fe}_3\text{O}_4@\text{SiO}_2@\text{Ru}$ photocatalysts' irradiation effect and not by the other individual constituents of the $\text{Fe}_3\text{O}_4@\text{SiO}_2@\text{Ru}$ composite. Furthermore, the effects of other practical parameters, pH of the azo dye solution, azo dye concentration in the solution, and amount or dose of photocatalyst in the degradation solution were examined on the dye degradation efficiency. Also, the kinetics of the photocatalytic reaction and the reuse of $\text{Fe}_3\text{O}_4@\text{SiO}_2@\text{Ru}$ HMCs were evaluated, presented, and discussed.

3.10.1. Influence of pH on MO and MR Degradation. The pH is critical in photocatalytic degradation because it affects the release of protons and the formation of hydroxyl radicals. Various sectors, such as dye manufacturing and surface coating, discharge their effluent into water sources at different stages. As a result, determining the effect of pH on pollutant photodegradation in the organic dye mechanism is critical. This involves hydroxyl radical attack, direct electron reduction in the conducting band, and positive hole direct oxidation [60]. Using a concentration of 10 mg/mL dye solution and 1 g/L of $\text{Fe}_3\text{O}_4@\text{SiO}_2@\text{Ru}$ photocatalyst, the pH effect was studied at various pH values. The pH of the solution was modified using diluted sodium hydroxide (NaOH) or hydrochloric acid (HCl). At pHs 4, 7, and 10, the photocatalytic degradation of azo dyes was measured and the respective degradation results are presented in Figure 11. As the pH increases from 4 to 10, the azo dye degradation efficiencies decreased, indicating that pH plays a large part in the degradation of MO and MR. In the acid medium, the most degradation is found. In addition, MO dye was found to degrade faster than MR dye. As a result of the effective electron transfer, the interaction of the photocatalyst ions with the positive holes resulted in the generation of a significant number of hydroxyl radicals and the formation of a rich surface complex bond [61]. The photodegradation was reduced with higher pH values; this is due to the coulombic repulsion between the hydroxyl (OH^-) anions and the positive charged oxide surface, which is caused by the diffusion of the further generated OH^- anions on the catalyst surface. The increased pH can also cause a cathodic displacement of the composite catalyst valence band position, reducing the holes' potential to oxidize [62].

3.10.2. Effect of Variation in Dosage of $\text{Fe}_3\text{O}_4@\text{SiO}_2@\text{Ru}$ Photocatalyst. The optimal amount of catalyst loading is the decisive step in scaling up the photocatalytic process since it affects both the process's economy and the downstream processing needed to remove the photocatalyst from the reaction mixture. The effect of $\text{Fe}_3\text{O}_4@\text{SiO}_2@\text{Ru}$ photocatalyst loading on the degradation of MO and MR dyes at concentrations ranging from 0.2 to 1.0 g/L was investigated under a constant of experimental conditions of 10 mg/mL of MO/MR dye concentration and pH 4. Figure 12 illustrates the effect of the photocatalyst loading on the degradation efficiency. As expected, the amount of $\text{Fe}_3\text{O}_4@\text{SiO}_2@\text{Ru}$ applied to the reaction medium had an impact on the efficiency of the operation. The percentage of azo dye removal increased linearly with $\text{Fe}_3\text{O}_4@\text{SiO}_2@\text{Ru}$ loading and reached a maximum of 0.8 g/L. Beyond that, the removal percentage is almost constant as the $\text{Fe}_3\text{O}_4@\text{SiO}_2@\text{Ru}$ dose is increased. The observed increase in decolorization efficiency is explained by a rise in the density (number) of active sites on the catalyst, which leads to an increase in the active radicals (hydroxyl and superoxide) that trigger the degradation reaction. As the catalyst loading is increased, the $\text{Fe}_3\text{O}_4@\text{SiO}_2@\text{Ru}$ particles serve as a barrier to incident visible irradiation, preventing it from reaching other particles. Another possibility is that the catalyst NPs aggregate due to their high surface energy and surface area. As a result,

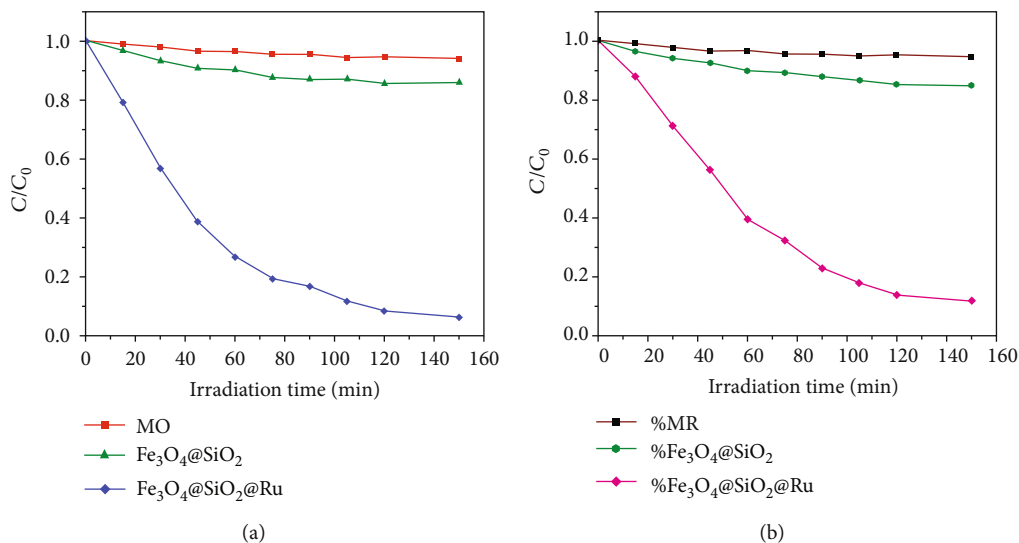


FIGURE 10: Photocatalytic degradation of (a) MO and (b) MR by $\text{Fe}_3\text{O}_4@SiO_2@Ru$ HMCs.

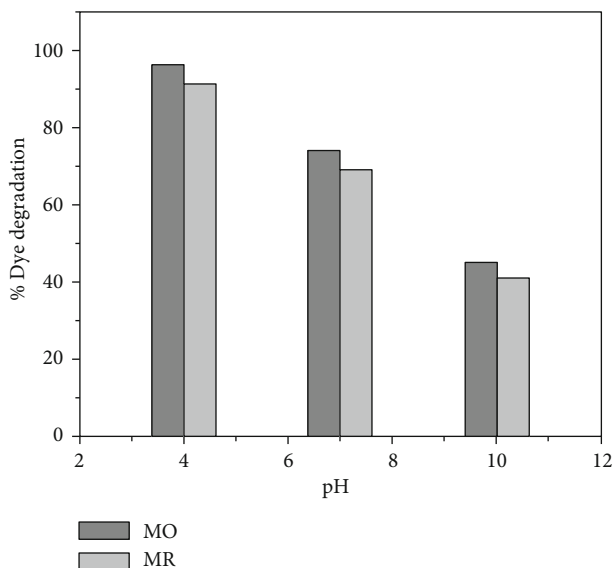


FIGURE 11: Effect of pH on the degradation of MO and MR.

the effective surface area of the catalyst decreases, resulting in a decrease in decolorization performance.

3.10.3. The Effect of Azo Dye Concentration. The rate at which a dye or pollutant degrades photocatalytically depends on its concentration, nature, and the role of other compounds in the polluted water. The concentration of dye has an effect on the photodegradation efficiency of MO and MR dyes, as seen in Figures 13(a) and 13(b). At concentrations of 10, 20, 30, and 40 mg/L, the degradation efficiencies were determined by keeping a constant dose of 1 g/L of $\text{Fe}_3\text{O}_4@SiO_2@Ru$ photocatalyst and a constant pH of 4. The results showed that the degradation efficiencies for MO were observed as 67, 78, 84, and 93 percent, respectively, and for MR as 60, 73, 82, and 88 percent, respectively. The low concentration of azo dye, 10 mg/L, provides the highest

performance, while the high concentration activates the photocatalytic process but slows down its degradation rate. A possible way is that as the initial concentration of the dye increases, the azo dye molecules get adsorb on the $\text{Fe}_3\text{O}_4@SiO_2@Ru$ photocatalyst surface, which absorbs a significant amount of visible light. This leads to a saturated photocatalyst's surface (the MO/MR dye molecules completely occupy the active sites of the $\text{Fe}_3\text{O}_4@SiO_2@Ru$ photocatalyst), and the number of photons getting to the $\text{Fe}_3\text{O}_4@SiO_2@Ru$ surface decreases, which is induced by the high concentration of the azo dye. This also diminishes the generation of hydroxyl radicals, resulting in inactivation of the photocatalytic degradation reaction. In addition, the nature of the dye is used to effectively bind to the photocatalyst surface, which makes it capable of removing dyes from the solution more efficiently.

3.10.4. Kinetics of MO/MR Dye Degradation. The kinetics of photocatalytic degradation of azo dyes, MO and MR, by $\text{Fe}_3\text{O}_4@SiO_2@Ru$ catalysts was estimated by pseudo-first-order kinetics, which is given by the following equation:

$$-\ln \left(\frac{C}{C_0} \right) = kt, \quad (3)$$

where C_0 indicates the initial concentration of the MO/MR dye (mg/L), C is the concentration of the MO/MR dye after irradiation time " t ," and k is the degradation rate constant (min^{-1}). The $-\ln(C/C_0)$ is plotted as a function of the irradiation time for different MO/MR dye concentrated samples, and the corresponding curves are displayed in Figures 13(c) and 13(d). It can be seen from the kinetic plots that a linear relationship between $-\ln(C/C_0)$ and irradiation time was found for both MO and MR azo dyes. The photocatalytic degradation of the azo dyes follows the pseudo first-order kinetics of the Langmuir-Hinshelwood model [63]. The degradation rate constants are estimated using the slopes of regression lines and are listed in Table 1.

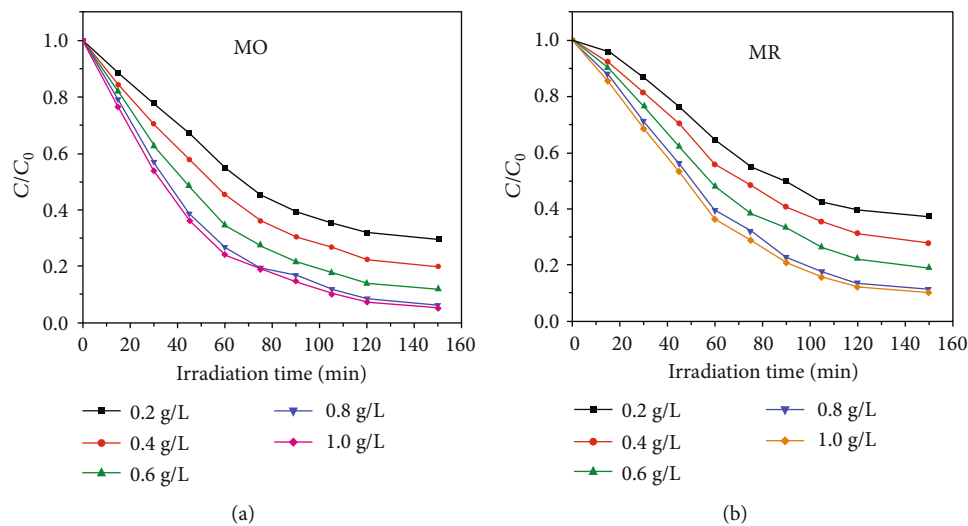


FIGURE 12: Effect of variation in dosage of photocatalyst on degradation of (a) MO and (b) MB.

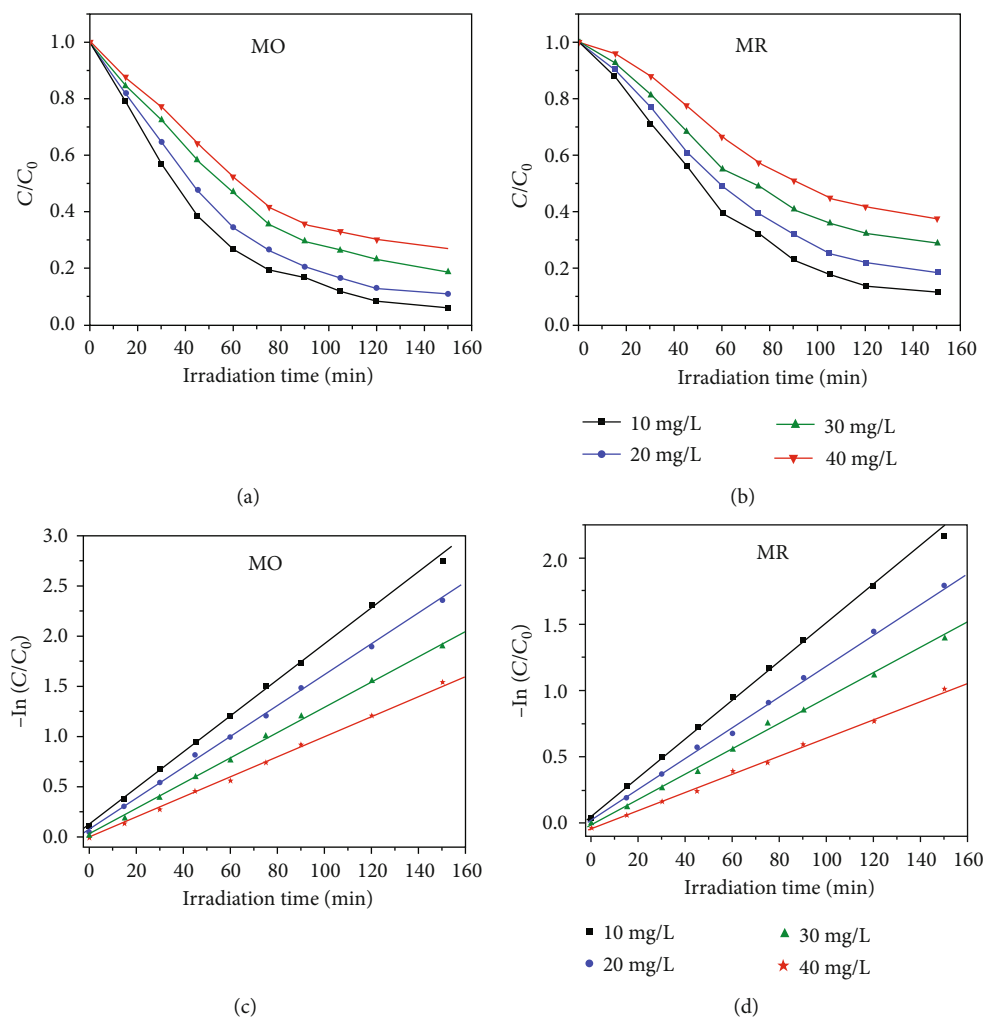


FIGURE 13: Effect of variation in concentration on dye degradation of (a) MO & (b) MR and kinetic plots of $-\ln(C/C_0)$ vs. irradiation time for (c) MO & (d) MR.

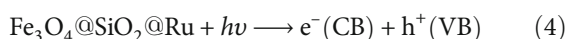
TABLE 1: Kinetic parameters for photocatalytic degradation of MO and MR dyes.

Azo dye	Azo dye conc. (mg/L ⁻¹)	k (min ⁻¹)	R ²
MO	10	0.0428	0.994
	20	0.0382	0.990
	30	0.0311	0.983
	40	0.0244	0.979
MR	10	0.0338	0.992
	20	0.0282	0.988
	30	0.0214	0.982
	40	0.0158	0.980

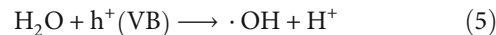
The degradation rate constants are progressively decreased as the dye concentration increased, which corresponds to the Langmuir–Hinshelwood model. It states that azo dye is first adsorbed on the photocatalyst surface and then degraded by photon irradiation. When the initial reactant concentration is reached, the molecules accumulate on the photocatalyst surface and quench the excited molecules [64]. In addition, high adsorption of the incident photon occurs as a result of an increase in the initial concentration, resulting in a decrease in the reaction rate constant [65]. The R² values (Table 1) clearly show that azo dyes undergo photocatalytic degradation in a manner consistent with pseudo first-order reaction kinetics.

Tables 2 and 3 summarize a comparative analysis of photocatalytic degradation of MO and MR dyes, respectively, using different photocatalysts based on a literature survey. Our current research work demonstrates that the synthesized Fe₃O₄@SiO₂@Ru HMNCs are potential candidates for organic dye removal.

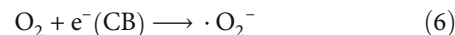
3.10.5. Photocatalytic Degradation Mechanism. Most synthesized azo dyes or organic pollutant dyes are highly soluble in water and very stable in aqueous solutions. Therefore, these color pollutants released from the dye industries are of great concern to environmental water pollution. To eliminate organic dye pollutants, the reaction mechanism provides significant support for photocatalytic reactions that occur during the photodegradation process. The superior photocatalytic efficiency of Fe₃O₄@SiO₂@Ru HMCs is due to the highly dispersed small-sized Ru NPs (~3 nm) on the surface of silica-coated magnetic microspheres. This enabled MO/MR molecules to easily enter the Ru NPs that serve as electron relays for the photodegradation reaction mechanism. The potential photodegradation process of azo dyes is represented schematically in Figure 14. As the Fe₃O₄@SiO₂@Ru photocatalyst is irradiated with visible light, Ru NPs absorb energy and the electrons (e⁻) in the valance band (VB) excite to the conduction band (CB) leaving a hole (h⁺). As a result, electron-hole pairs called excitons (e⁻/h⁺) are produced; this is the initial step to start the photocatalytic degradation process.



Since photocatalysts and azo dyes are in an aqueous solution, the water (H₂O) molecules absorbed by the Fe₃O₄@SiO₂@Ru photocatalyst surface react with the h⁺s of VB (photooxidation reaction) to produce hydroxyl (·OH) free radicals which are highly reactive species.

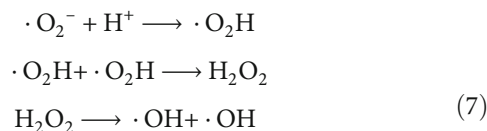


On the other hand, the e⁻ in CB reacts with oxygen (O₂) (photoreduction reaction) to generate superoxide anion radical (·O₂⁻) through transfer of trapped e⁻ from Ru surface as shown in Figure 14.



These photooxidation and photoreduction reactions are demonstrated in Equations (5) and (6), which eliminate the possibility of an electron–hole recombination process.

In addition, ·O₂⁻ radicals produced may react with H⁺ to form H₂O₂, and this H₂O₂ is further activated by electrons and convert to form ·OH radicals. The generated reactive species, ·O₂⁻ and ·OH, have a high oxidative ability and can potentially degrade azo dyes into smaller intermediates or low molecular weight by-products and to the final degradation products, CO₂ and H₂O. The possible reactions which occur in the photocatalytic degradation process are proposed below.



3.11. Evaluation of the Recyclability of the Photocatalysts. For any type of catalyst, reusability is a critical theme to its successful use. The usability is sought with a greener and environmentally sustainable solution, as it eliminates waste and thus cuts maintenance costs. Hence, in order to investigate the recyclability, Fe₃O₄@SiO₂@Ru HMCs were filtered from the reaction mixture. Following that, the HMCs were washed with deionized water and EtOH and then dried in an oven set at 100°C for each cycle. After recovering the composite catalyst, it was used for photodegradation of MO and MR dyes under similar experimental parameters. The Fe₃O₄@SiO₂@Ru composite's photocatalytic activity was evaluated six times. As shown in Figure 15, also after six reuses, the composite catalyst maintained its photocatalytic activity, and the azo dye degradation performance was nearly identical. The Fe₃O₄@SiO₂@Ru composite's recyclability is a result of its stability and resistance to photocorrosion [65]. As a result of Fe₃O₄@SiO₂@Ru composite's recyclable nature, it can be used as an effective photocatalyst for organic dye degradation.

TABLE 2: Comparison of photodegradation of MO using different photocatalysts.

Photocatalysts	Preparation method	Light irradiated	Lamp power (W)	Catalyst dose	Irradiation time (min)	Degradation (%)	Ref.
QD-sensitized Cds-Bi ₂ WO ₆	Hydrothermal approach	Visible light	500 W Xe lamp	10 mg/L	180	97	[66]
α -Bi ₂ O ₃	Sol gel	Visible light	500 W xenon source	16.4 mg/L	240	93	[67]
ZnO nanomushrooms	Combustion	UV light	—	0.25 g/ 100 mL	210	92	[68]
Transition metal-doped ZnO NPs	Thermal decomposition	UV light	—	0.1 g	150	91	[69]
CeO ₂ and Fe-doped CeO ₂	Precipitation combined with impregnation	Visible light	50-watt halogen lamp	0.025 mM	120	—	[70]
TiO ₂ NPs	Sol gel	Visible light	500 W xenon lamp	10 mg	240	67	[71]
La ₂ NiO ₄ /ZnO	Impregnation	Solar light	750 W m ⁻² radiometer	50 mg	60	90	[72]
TiO ₂ /biochar	Hydrolysis	UV light	500 W	10 mg	150	96.88	[73]
Ag-AgI/Bi ₃ O ₄ Cl	Wet chemical	Visible light	5 W LED lamp (80 mW·cm ⁻²)	20 mg/L	180	60	[74]
Fe ₃ O ₄ @SiO ₂ @Ru HMNCs	Multistep wet chemical process	UV light	8 W Hg lamp	10 mg	150	95	PM

TABLE 3: Comparison of photodegradation of MR using different photocatalysts.

Photocatalysts	Preparation method	Light irradiated	Lamp power (W)	Catalyst dose	Irradiation time (min)	Degradation (%)	Ref.
Titania-alumina-zinc ferrite	Multistep wet chemical process	UV light	8 W	100 mg	15 hrs	90	[75]
NiCo ₂ O ₄ fibers	C-precipitation decomposition method	Visible light	500 W xenon lamp	0.12 g	120	95	[76]
TiO ₂	Pechini method	UV light	15 W mercury vapor lamp	20 mg/L	24 hrs	89	[77]
WO ₃ thin films	Chemical spray pyrolysis	Visible light	500 W	0.125 M	160	97	[78]
Fe ₃ O ₄ NPs	Sonochemical	UV light	8 W-Hg vapor lamp	0.075 g/L	60	60	[79]
Cu ₂ O/ZnO nanocomposite	Coprecipitation & thermal decomposition	Sunlight	Sunlight	18 mg/L	180	90	[80]
Porous zinc hydroxide	Sol-gel	Visible light	3 W white LED lamp	2.5 g/L	180	89	[81]
CNT/ZnO nanocomposite	Sol-gel	Sunlight	Sun light	20 mg/L	30	80	[82]
Fe ₃ O ₄ @SiO ₂ @Ru HMNCs	Multistep wet chemical process	UV light	8 W Hg lamp	10 mg	150	91	PM

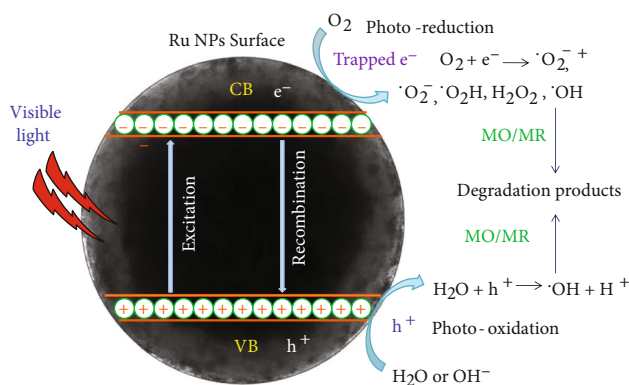


FIGURE 14: Mechanism of photocatalytic degradation of MO/MR dyes by $\text{Fe}_3\text{O}_4@\text{SiO}_2@\text{Ru}$ HMCs.

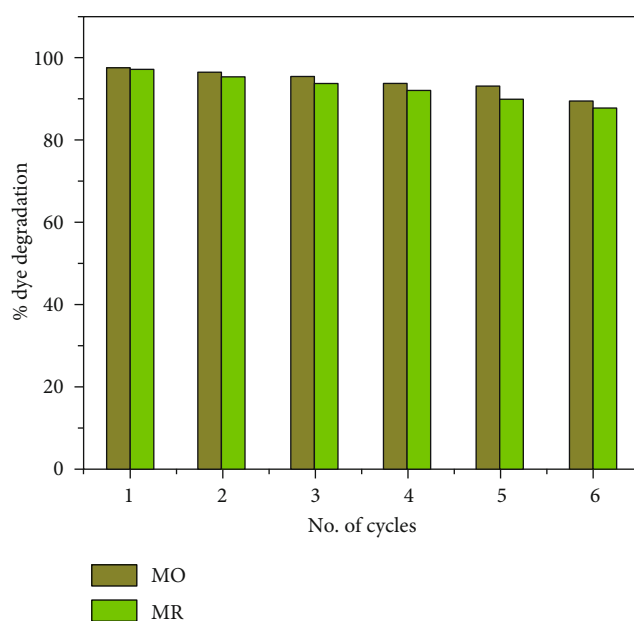


FIGURE 15: Photocatalytic activity of $\text{Fe}_3\text{O}_4@\text{SiO}_2@\text{Ru}$ HMC catalysts on repeated cycles.

4. Conclusions

In this work, a facile and reproducible method was developed for synthesizing $\text{Fe}_3\text{O}_4@\text{SiO}_2@\text{Ru}$ core-shell HMCs by a three-step method. The presynthesized Ru NPs (~ 3 nm) were immobilized onto the surface of $\text{Fe}_3\text{O}_4@\text{SiO}_2$ MMSs by applying an electrostatic method to obtain $\text{Fe}_3\text{O}_4@\text{SiO}_2@\text{Ru}$ HMCs. Different characterization techniques such as XRD, FT-IR, TEM, EDS, XPS, BET, PL, UV-Vis DRS, and VSM were performed to study morphology, chemical, optical, and magnetic properties of $\text{Fe}_3\text{O}_4@\text{SiO}_2@\text{Ru}$ HMCs. The photocatalytic efficiency of the synthesized Ru-decorated magnetic composite was examined for degradation of MO and MR azo dyes in aqueous solution under visible light irradiation by varying several working parameters without any additional reductant/oxidant. The results indicate that $\text{Fe}_3\text{O}_4@\text{SiO}_2@\text{Ru}$ HMCs showed excellent photocatalytic degradation of azo

dyes. Based on the above findings and discussion, the photocatalytic activity of $\text{Fe}_3\text{O}_4@\text{SiO}_2@\text{Ru}$ HMCs is due to the synergistic effects of the highly dispersed small-sized Ru NPs, the sandwich silicon layers' strong adsorption nature, and the $\text{Fe}_3\text{O}_4@\text{SiO}_2@\text{Ru}$ HMCs' excellent dispersion. Accordingly, a suitable degradation mechanism of organic dyes was proposed for the photocatalytic process. The developed $\text{Fe}_3\text{O}_4@\text{SiO}_2@\text{Ru}$ HMCs are easily isolated from the solution and reused using an external magnetic field, and also, their photocatalytic activity did not vary significantly up to 6 cycles. Photocatalysis results reveal that $\text{Fe}_3\text{O}_4@\text{SiO}_2@\text{Ru}$ HMCs are potential candidates as the most effective photocatalysts for degradation of organic dyes and so as applicants for environmental protection.

Data Availability

The data used to support the findings of this study are included within the article.

Conflicts of Interest

The authors declare no conflict of interest.

References

- [1] T. S. Natarajan, H. C. Bajaj, and R. J. Tayade, "Recent advances based on the synergetic effect of adsorption for removal of dyes from waste water using photocatalytic process," *Journal of Environmental Sciences*, vol. 65, pp. 201–222, 2018.
- [2] T. S. Natarajan, K. Natarajan, H. C. Bajaj, and R. J. Tayade, "Study on identification of leather industry wastewater constituents and its photocatalytic treatment," *International journal of Environmental Science and Technology*, vol. 10, no. 4, pp. 855–864, 2013.
- [3] A. E. Ghaly, R. Ananthashankar, M. Alhattab, and V. V. Ramakrishnan, "Production, characterization and treatment of textile effluents: a critical review," *Journal of Chemical Engineering & Process Technology*, vol. 5, pp. 1–6, 2014.
- [4] M. Rani and U. Shanker, "Insight in to the degradation of bisphenol A by doped $\text{ZnO}@\text{ZnHCF}$ nanocubes: High photocatalytic performance," *Journal of Colloid Science*, vol. 530, pp. 16–28, 2018.
- [5] M. Rani, U. Rachna, and J. Shanker, "Mineralization of carcinogenic anthracene and phenanthrene by sunlight active bimetallic oxides nanocomposites," *Journal of Colloid Science*, vol. 555, pp. 676–688, 2019.
- [6] A. Ahmad, S. H. Mohd-Setapar, C. S. Chuong et al., "Recent advances in new generation dye removal technologies: novel search for approaches to reprocess wastewater," *RSC Advances*, vol. 5, no. 39, pp. 30801–30818, 2015.
- [7] H. Lachheb, E. Puzenat, A. Houas et al., "Photocatalytic degradation of various types of dyes (Alizarin S, Crocein Orange G, Methyl Red, Congo Red, Methylene Blue) in water by UV-irradiated titania," *Applied Catalysis B: Environmental*, vol. 39, no. 1, pp. 75–90, 2002.
- [8] M. Rani and U. Shanker, "Sun-light driven rapid photocatalytic degradation of methylene blue by poly(methyl methacrylate)/metal oxide nanocomposites," *Colloids and Surfaces A: Physicochemical and Engineering Aspects*, vol. 559, pp. 136–147, 2018.

- [9] U. Shanker, M. Rani, and V. Jassal, "Degradation of hazardous organic dyes in water by nanomaterials," *Environmental Chemistry Letters*, vol. 15, no. 4, pp. 623–642, 2017.
- [10] P. K. Boruah, S. Szunerits, R. Boukherroub, and M. R. Das, "Magnetic Fe₃O₄@V₂O₅/rGO nanocomposite as a recyclable photocatalyst for dye molecules degradation under direct sunlight irradiation," *Chemosphere*, vol. 191, pp. 503–513, 2018.
- [11] S. Mondal, M. E. De Anda Reyes, and U. Pal, "Plasmon induced enhanced photocatalytic activity of gold loaded hydroxyapatite nanoparticles for methylene blue degradation under visible light," *RSC Advances*, vol. 7, no. 14, pp. 8633–8645, 2017.
- [12] P. K. Boruah, P. Borthakur, G. Darabdhara et al., "Sunlight assisted degradation of dye molecules and reduction of toxic Cr(vi) in aqueous medium using magnetically recoverable Fe₃O₄/reduced graphene oxide nanocomposite," *RSC Advances*, vol. 6, no. 13, pp. 11049–11063, 2016.
- [13] C. Chen, Z. Ma, S. Zhou, T. Li, and X. Sun, "Cobalt-Tetracarboxyl-Phthalocyanine Linked with Fe₃O₄/Chitosan Microspheres—Efficient Catalyst for Dye Degradation," *Catalysis Letters*, vol. 147, no. 9, pp. 2399–2409, 2017.
- [14] F. Moradnia, S. Taghavi Fardood, A. Ramazani, S. Osali, and I. Abdolmaleki, "Green sol-gel synthesis of CoMnCrO₄ spinel nanoparticles and their photocatalytic application," *Micro & Nano Letters*, vol. 15, no. 10, pp. 674–677, 2020.
- [15] K. Atrak, A. Ramazani, and S. Taghavi Fardood, "Green synthesis of Zn_{0.5}Ni_{0.5}AlFeO₄ magnetic nanoparticles and investigation of their photocatalytic activity for degradation of reactive blue 21 dye," *Environmental Technology*, vol. 41, no. 21, pp. 2760–2770, 2020.
- [16] K. S. Ranjith, P. Manivel, R. T. Rajendrakumar, and T. Uyar, "Multifunctional ZnO nanorod-reduced graphene oxide hybrids nanocomposites for effective water remediation: Effective sunlight driven degradation of organic dyes and rapid heavy metal adsorption," *Chemical Engineering Journal*, vol. 325, pp. 588–600, 2017.
- [17] H. Chen, K. Shen, J. Chen, X. Chen, and Y. Li, "Hollow-ZIF-templated formation of a ZnO@C-N-Co core-shell nanostructure for highly efficient pollutant photodegradation," *Journal of Materials Chemistry A*, vol. 5, no. 20, pp. 9937–9945, 2017.
- [18] Y. Wang, Q. Wang, X. Zhan, F. Wang, M. Safdar, and J. He, "Visible light driven type II heterostructures and their enhanced photocatalysis properties: a review," *Nanoscale*, vol. 5, no. 18, pp. 8326–8339, 2013.
- [19] Y. H. Deng, Y. Cai, Z. K. Sun et al., "Multifunctional Mesoporous Composite Microspheres with Well-Designed Nanostructure: A Highly Integrated Catalyst System," *Journal of the American Chemical Society*, vol. 132, no. 24, pp. 8466–8473, 2010.
- [20] X. Liu, D. Wang, and Y. Li, "Synthesis and catalytic properties of bimetallic nanomaterials with various architectures," *Nano Today*, vol. 7, no. 5, pp. 448–466, 2012.
- [21] H. Wang, J. Shen, Y. Li et al., "Porous Carbon Protected Magnetite and Silver Hybrid Nanoparticles: Morphological Control, Recyclable Catalysts, and Multicolor Cell Imaging," *ACS Applied Materials & Interfaces*, vol. 5, no. 19, pp. 9446–9453, 2013.
- [22] C. Santhosh, P. Kollu, S. Doshi et al., "Adsorption, photodegradation and antibacterial study of graphene-Fe₃O₄ nanocomposite for multipurpose water purification application," *RSC Advances*, vol. 4, no. 54, pp. 28300–28308, 2014.
- [23] S. Chidambaram, B. Pari, N. Kasi, and S. Muthusamy, "ZnO/Ag heterostructures embedded in Fe₃O₄ nanoparticles for magnetically recoverable photocatalysis," *Journal of Alloys and Compounds*, vol. 665, pp. 404–410, 2016.
- [24] E. Alzahrani, "Photodegradation of Eosin Y Using Silver-Doped Magnetic Nanoparticles," *International Journal of Analytical Chemistry*, vol. 2015, Article ID 797606, 11 pages, 2015.
- [25] H. Liang, H. Niu, P. Li et al., "Multifunctional Fe₃O₄@C@Ag hybrid nanoparticles: Aqueous solution preparation, characterization and photocatalytic activity," *Materials Research Bulletin*, vol. 48, no. 7, pp. 2415–2419, 2013.
- [26] W. Wu, Q. He, and C. Jiang, "Magnetic Iron Oxide Nanoparticles: Synthesis and Surface Functionalization Strategies," *Nanoscale Research Letters*, vol. 3, no. 11, pp. 397–415, 2008.
- [27] Y. Liu, L. Li, S. Liu, C. Xie, and S. Yu, "Synthesis of silanized magnetic Ru/Fe₃O₄@SiO₂ nanospheres and their high selectivity to prepare cis-pinane," *RSC Advances*, vol. 6, no. 84, pp. 81310–81317, 2016.
- [28] Q. Zhang, G. Meng, J. Wu, D. Li, and Z. Liu, "Study on enhanced photocatalytic activity of magnetically recoverable Fe₃O₄@C@TiO₂ nanocomposites with core-shell nanostructure," *Optical Materials*, vol. 46, pp. 52–58, 2015.
- [29] A. P. Kumar, D. Bilehal, A. Tadesse, and D. Kumar, "Photocatalytic degradation of organic dyes: Pd- γ -Al₂O₃ and PdO- γ -Al₂O₃ as potential photocatalysts," *RSC Advances*, vol. 11, no. 11, pp. 6396–6406, 2021.
- [30] S. Gautam, H. Agrawal, M. Thakur et al., "Metal oxides and metal organic frameworks for the photocatalytic degradation: A review," *Journal of Environmental Chemical Engineering*, vol. 8, no. 3, p. 103726, 2020.
- [31] A. P. Kumar, B. P. Kumar, A. B. V. K. Kumar, B. T. Huy, and Y. I. Lee, "Preparation of palladium nanoparticles on alumina surface by chemical co-precipitation method and catalytic applications," *Applied Surface Science*, vol. 265, pp. 500–509, 2013.
- [32] A. Praveen Kumar, F. Ahmed, G. Shalendra Kumar, K. Anuradha, B. P. Harish, and K. Y.-I. Lee, "Synthesis of magnetically separable Fe₃O₄@Ru nanocomposite for efficient photocatalytic degradation of methylene blue," *Journal of Cluster Science*, 2021.
- [33] A. Cid and J. Simal-Gandara, "Synthesis, Characterization, and Potential Applications of Transition Metal Nanoparticles," *Journal of Inorganic and Organometallic Polymers and Materials*, vol. 30, no. 4, pp. 1011–1032, 2020.
- [34] W. Jin and G. Maduraiveeran, "Recent advances of porous transition metal-based nanomaterials for electrochemical energy conversion and storage applications," *Materials Today Energy*, vol. 13, pp. 64–84, 2019.
- [35] A. P. Kumar, B. T. Huy, B. P. Kumar et al., "Novel dithiols as capping ligands for CdSe quantum dots: optical properties and solar cell applications," *Journal of Materials Chemistry C*, vol. 3, no. 9, pp. 1957–1964, 2015.
- [36] A. P. Kumar, J. H. Kim, T. D. Thanh, and Y. I. Lee, "Chiral zirconia magnetic microspheres as a new recyclable selector for the discrimination of racemic drugs," *Journal of Materials Chemistry*, vol. 1, no. 38, pp. 4909–4915, 2013.
- [37] M. S. S. Danish, L. L. Estrella, I. M. A. Alemaida et al., "Photocatalytic Applications of Metal Oxides for Sustainable Environmental Remediation," *Metalsmith*, vol. 11, no. 1, p. 80, 2021.
- [38] A. A. Yaqoob, H. Ahmad, T. Parveen et al., "Recent Advances in Metal Decorated Nanomaterials and Their Various

- Biological Applications: A Review,” *Frontiers in Chemistry*, vol. 8, p. 341, 2020.
- [39] M. Sait Izgi, M. Ş. Ece, H. Ç. Kazici, Ö. Şahin, and E. Onat, “Hydrogen production by using Ru nanoparticle decorated with $\text{Fe}_3\text{O}_4/\text{SiO}_2\text{-NH}_2$ core-shell microspheres,” *International Journal of Hydrogen Energy*, vol. 45, no. 55, pp. 30415–30430, 2020.
- [40] Y. Liu, M. Lv, H. Y. Li et al., “Synthesis of a highly active amino-functionalized $\text{Fe}_3\text{O}_4/\text{SiO}_2/\text{APTS}/\text{Ru}$ magnetic nanocomposite catalyst for hydrogenation reactions,” *Applied Organometallic Chemistry*, vol. 33, no. 4, article e4686, 2019.
- [41] Q. Zhang, L. G. Yu, C. C. Xu et al., “Preparation of highly efficient and magnetically recyclable $\text{Fe}_3\text{O}_4/\text{C}/\text{Ru}$ nanocomposite for the photocatalytic degradation of methylene blue in visible light,” *Applied Surface Science*, vol. 483, pp. 241–251, 2019.
- [42] S. Xuan, Y. X. J. Wang, J. C. Yu, and K. C. F. Leung, “Preparation, Characterization, and Catalytic Activity of Core/Shell $\text{Fe}_3\text{O}_4/\text{Polyaniline}/\text{Au}$ Nanocomposites,” *Langmuir*, vol. 25, no. 19, pp. 11835–11843, 2009.
- [43] S. H. Joo, J. Y. Park, J. R. Renzas, D. R. Butcher, W. Huang, and G. A. Somorjai, “Size Effect of Ruthenium Nanoparticles in Catalytic Carbon Monoxide Oxidation,” *Nano Letters*, vol. 10, no. 7, pp. 2709–2713, 2010.
- [44] L. L. Sun, W. Wu, S. L. Yang et al., “Template and Silica Interlayer Tailorable Synthesis of Spindle-like Multilayer $\alpha\text{-Fe}_2\text{O}_3/\text{Ag}/\text{SnO}_2$ Ternary Hybrid Architectures and Their Enhanced Photocatalytic Activity,” *ACS Applied Materials & Interfaces*, vol. 6, no. 2, pp. 1113–1124, 2014.
- [45] P. K. Vanama, A. Kumar, S. R. Gijnjupalli, and V. R. C. Komandur, “Vapor-phase hydrogenolysis of glycerol over nanostructured Ru/MCM-41 catalysts,” *Catalysis Today*, vol. 250, pp. 226–238, 2015.
- [46] S. Sadeghi, H. Azhdari, H. Arabi, and A. Z. Moghaddam, “Surface modified magnetic Fe_3O_4 nanoparticles as a selective sorbent for solid phase extraction of uranyl ions from water samples,” *Journal of Hazardous Materials*, vol. 215–216, pp. 208–216, 2012.
- [47] Y. Zhao, J. Li, L. Zhao et al., “Synthesis of amidoxime-functionalized $\text{Fe}_3\text{O}_4/\text{SiO}_2$ core-shell magnetic microspheres for highly efficient sorption of U(VI),” *Chemical Engineering Journal*, vol. 235, pp. 275–283, 2014.
- [48] H. Chen, C. Deng, and X. Zhang, “Synthesis of $\text{Fe}_3\text{O}_4/\text{SiO}_2/\text{PMMA}$ Core-Shell-Shell Magnetic Microspheres for Highly Efficient Enrichment of Peptides and Proteins for MALDI-ToF MS Analysis,” *Angewandte Chemie, International Edition*, vol. 49, no. 3, pp. 607–611, 2010.
- [49] M. Guo, G. Lan, J. Peng, M. Li, Q. Yang, and C. Li, “Enhancing the catalytic activity of Ru NPs deposited with carbon species in yolk-shell nanostructures,” *Journal of Materials Chemistry A*, vol. 4, no. 28, pp. 10956–10963, 2016.
- [50] S. Kumar, S. T. B. Kumar, A. Baruah, and V. Shanker, “Synthesis of Magnetically Separable and Recyclable g-C₃N₄- Fe_3O_4 Hybrid Nanocomposites with Enhanced Photocatalytic Performance under Visible-Light Irradiation,” *Journal of Physical Chemistry C*, vol. 117, no. 49, pp. 26135–26143, 2013.
- [51] O. V. Manaenkov, J. J. Mann, O. V. Kislitza et al., “Ru-Containing Magnetically Recoverable Catalysts: A Sustainable Pathway from Cellulose to Ethylene and Propylene Glycols,” *ACS Applied Materials & Interfaces*, vol. 8, no. 33, pp. 21285–21293, 2016.
- [52] B. Lin, K. Wei, X. Ma, J. Lin, and J. Ni, “Study of potassium promoter effect for Ru/AC catalysts for ammonia synthesis,” *Catalysis Science & Technology*, vol. 3, no. 5, p. 1367, 2013.
- [53] N. Cherkasov, V. Jadvani, J. Mann et al., “Hydrogenation of bio-oil into higher alcohols over Ru/ $\text{Fe}_3\text{O}_4\text{-SiO}_2$ catalysts,” *Fuel Processing Technology*, vol. 167, pp. 738–746, 2017.
- [54] J. Miao, X. Zhao, Y.-X. Zhang, and Z.-H. Liu, “Feasible synthesis of hierarchical porous MgAl-borate LDHs functionalized $\text{Fe}_3\text{O}_4/\text{SiO}_2$ magnetic microspheres with excellent adsorption performance toward Congo red and Cr(VI) pollutants,” *Journal of Alloys and Compounds*, vol. 861, p. 157974, 2021.
- [55] J. Coulter and D. Birnie, “Assessing Tauc Plot Slope Quantification: ZnO Thin Films as a Model System,” *Physica Status Solidi B*, vol. 255, no. 3, pp. 1–7, 2018.
- [56] A. Nikokavoura and C. Trapalis, “Graphene and g-C₃N₄ based photocatalysts for NO_x removal: A review,” *Applied Surface Science*, vol. 430, pp. 18–52, 2018.
- [57] Z. Zhao, Y. Sun, and F. Dong, “Graphitic carbon nitride based nanocomposites: a review,” *Nanoscale*, vol. 7, no. 1, pp. 15–37, 2015.
- [58] B. Prajapati, S. Kumar, M. Kumar, S. Chatterjee, and A. K. Ghosh, “Investigation of the physical properties of Fe:TiO₂-diluted magnetic semiconductor nanoparticles,” *Journal of Materials Chemistry C*, vol. 5, no. 17, pp. 4257–4267, 2017.
- [59] S. J. Guo, S. J. Dong, and E. K. Wang, “A General Route to Construct Diverse Multifunctional $\text{Fe}_3\text{O}_4/\text{Metal}$ Hybrid Nanostructures,” *Chemistry—A European Journal*, vol. 15, no. 10, pp. 2416–2424, 2009.
- [60] A. Ajmal, I. Majeed, R. N. Malik, H. Idriss, and M. A. Nadeem, “Principles and mechanisms of photocatalytic dye degradation on TiO₂-based photocatalysts: a comparative overview,” *RSC Advances*, vol. 4, no. 70, pp. 37003–37026, 2014.
- [61] P. Ameta, A. Kumar, R. Ameta, and R. K. Malkani, “A comparative study of photocatalytic activity of some coloured semiconducting oxides,” *Iranian Journal of Chemistry and Chemical Engineering*, vol. 29, pp. 43–48, 2010.
- [62] I. Poullos, M. Kositzi, and A. Kouras, “Photocatalytic decomposition of triclopyr over aqueous semiconductor suspensions,” *Journal of Photochemistry and Photobiology A: Chemistry*, vol. 115, no. 2, pp. 175–183, 1998.
- [63] Y. Li, X. Li, J. Li, and J. Yin, “Photocatalytic degradation of methyl orange by TiO₂-coated activated carbon and kinetic study,” *Water Research*, vol. 40, no. 6, pp. 1119–1126, 2006.
- [64] A. V. Emeline, V. Ryabchuk, and N. Serpone, “Factors affecting the efficiency of a photocatalyzed process in aqueous metal-oxide dispersions,” *Journal of Photochemistry and Photobiology A: Chemistry*, vol. 133, no. 1–2, pp. 89–97, 2000.
- [65] Z. Lu, X. Zhao, Z. Zhu et al., “Enhanced Recyclability, Stability, and Selectivity of CdS/C/ Fe_3O_4 Nanoreactors for Orientation Photodegradation of Ciprofloxacin,” *Chemistry - A European Journal*, vol. 21, no. 51, pp. 18528–18533, 2015.
- [66] L. Ge and J. Liu, “Efficient visible light-induced photocatalytic degradation of methyl orange by QDs sensitized CdS-Bi₂WO₆,” *Applied Catalysis. B, Environmental*, vol. 105, no. 3–4, pp. 289–297, 2011.
- [67] S. Iyyapushpam, S. T. Nishanthi, and D. Pathinettam Padiyan, “Photocatalytic degradation of methyl orange using $\alpha\text{-Bi}_2\text{O}_3$ prepared without surfactant,” *Journal of Alloys and Compounds*, vol. 563, pp. 104–107, 2013.

- [68] R. Kumar, G. Kumar, and A. Umar, "ZnO nano-mushrooms for photocatalytic degradation of methyl orange," *Materials Letters*, vol. 97, pp. 100–103, 2013.
- [69] J. Kaur and S. Singhal, "Facile synthesis of ZnO and transition metal doped ZnO nanoparticles for the photocatalytic degradation of Methyl Orange," *Ceramics International*, vol. 40, no. 5, pp. 7417–7424, 2014.
- [70] D. Channei, B. Inceesungvorn, N. Wetchakun et al., "Photocatalytic degradation of methyl orange by CeO₂ and Fe-doped CeO₂ films under visible light irradiation," *Scientific Reports*, vol. 4, p. 5757, 2014.
- [71] J. Dhanalakshmi and D. P. Padiyan, "Photocatalytic degradation of methyl orange and bromophenol blue dyes in water using sol-gel synthesized TiO₂ nanoparticles," *Materials Research Express*, vol. 4, p. 095020, 2017.
- [72] H. Lahmar, M. Benamira, S. Douafer, L. Messaadia, A. Boudjerda, and M. Trari, "Photocatalytic degradation of methyl orange on the novel hetero-system La₂NiO₄/ZnO under solar light," *Chemical Physics Letters*, vol. 742, p. 137132, 2020.
- [73] L. Lu, R. Shan, Y. Shi, S. Wang, and H. Yuan, "A novel TiO₂/biochar composite catalysts for photocatalytic degradation of methyl orange," *Chemosphere*, vol. 222, pp. 391–398, 2019.
- [74] B. Xu, Y. Li, Y. Gao et al., "Ag-AgI/Bi₃O₄Cl for efficient visible light photocatalytic degradation of methyl orange: The surface plasmon resonance effect of Ag and mechanism insight," *Applied Catalysis. B, Environmental*, vol. 246, pp. 140–148, 2019.
- [75] P. P. Hankare, R. P. Patil, A. V. Jadhav, K. M. Garadkar, and R. Sasikala, "Enhanced photocatalytic degradation of methyl red and thymol blue using titania-alumina-zinc ferrite nanocomposite," *Applied Catalysis. B, Environmental*, vol. 107, no. 3–4, pp. 333–339, 2011.
- [76] Y. Wan, J. Chen, J. Zhan, and Y. Ma, "Facile synthesis of mesoporous NiCo₂O₄ fibers with enhanced photocatalytic performance for the degradation of methyl red under visible light irradiation," *Journal of Environmental Chemical Engineering*, vol. 6, no. 5, pp. 6079–6087, 2018.
- [77] P. C. Ribeiro, A. C. F. M. Costa, R. H. G. A. Kiminami, J. M. Sasaki, and H. L. Lira, "Synthesis of TiO₂ by the pechini method and photocatalytic degradation of methyl red," *Materials Research*, vol. 16, no. 2, pp. 468–472, 2013.
- [78] Y. M. Hunge, V. S. Mohite, S. S. Kumbhar, K. Y. Rajpure, A. V. Moholkar, and C. H. Bhosale, "Photoelectrocatalytic degradation of methyl red using sprayed WO₃ thin films under visible light irradiation," *Journal of Materials Science: Materials in Electronics*, vol. 26, no. 11, pp. 8404–8412, 2015.
- [79] R. V. Solomon, I. S. Lydia, J. P. Merlin, and P. Venuvanalingam, "Enhanced photocatalytic degradation of azo dyes using nano Fe₃O₄," *Journal of the Iranian Chemical Society*, vol. 9, no. 2, pp. 101–109, 2012.
- [80] Y. T. Gaim, G. M. Tesfamariam, G. Y. Nigussie, and M. E. Ashebir, "Synthesis, Characterization and Photocatalytic Activity of N-doped Cu₂O/ZnO Nanocomposite on Degradation of Methyl Red," *Journal of Composites Science*, vol. 3, no. 4, p. 93, 2019.
- [81] Z. Zhu, H. Luo, and R.-J. Wu, "Photocatalytic degradation of methyl red by porous zinc hydroxide under visible light irradiation," *Journal of the Chinese Chemical Society*, vol. 66, no. 7, pp. 713–718, 2019.
- [82] X. Wang, S. Yao, and X. Li, "Sol-gel Preparation of CNT/ZnO Nanocomposite and Its Photocatalytic Property," *Chinese Journal of Chemistry*, vol. 27, no. 7, pp. 1317–1320, 2009.